RSC Advances

PAPER

View Article Online
View Journal | View Issue

Cite this: *RSC Adv.*, 2020, **10**, 29051

Storage performance of Mg^{2+} substituted $NaMnPO_4$ with an olivine structure†

Tanya Boyadzhieva,[a] Violeta Koleva,[a] Rosica Kukeva,[a] Diana Nihtianova,[ab] Sonya Harizanova[a] and Radostina Stoyanova*[a]

Sodium manganese phospho-olivine, $NaMnPO_4$, is considered to be a higher-voltage alternative to the presently used iron-based electrode material, $NaFePO_4$, for sodium ion batteries. Irrespective of this advantage, the electrochemical performance of $NaMnPO_4$ is still far from what is desired. Herein we provide the first report on the storage performance of $NaMnPO_4$ having a structure modified by Mg^{2+} substitution. The Mg-substituted phospho-olivines are prepared on the basis of ionic exchange reactions involving the participation of Mg-substituted $KMnPO_4 \cdot H_2O$ dittmarites as structural template. Furthermore, the phosphate particles were covered with a thin layer (up to 5 nm) of activated carbon through ball-milling. The storage performance of phospho-olivines is analyzed in sodium and lithium half-ion cells, as well as in full-ion cells *versus* bio-mass derived activated carbon and spinel $Li_4Ti_5O_{12}$ as anodes. The compatibility of phospho-olivines with electrolytes is assessed by utilization of several types of lithium and sodium carbonate-based solutions. In sodium half-cell, the Mg-substituted phosphate displays a multi-phase mechanism of Na^+ intercalation in case when NaTFSI-based electrolyte is used. In lithium half-cell, the high specific capacity and rate capability is achieved for phospho-olivine cycled in $LiPF_6$-based electrolyte. This is a consequence of the occurrence of dual Li^+,Na^+ intercalation, which encompass nano-sized domains. The utilization of the Mg-substituted phospho-olivine in the full ion cell is demonstrated.

Received 30th June 2020
Accepted 30th July 2020

DOI: 10.1039/d0ra05698g

rsc.li/rsc-advances

1. Introduction

Sodium manganese phospho-olivine, $NaMnPO_4$, is considered to be an attractive alternative to the conventional iron-based electrode material, $NaFePO_4$, for sodium ion batteries.[1,2] This is a consequence from the high redox potential of the Mn^{2+}/Mn^{3+} ionic pair, thus reaching higher energy density.[1,3] Irrespective of this advantage, the studies on the electrochemical activity of $NaMnPO_4$ remain relatively fragmentary in comparison with that of $NaFePO_4$.[1,2] Recently, we have firstly demonstrated that $NaMnPO_4$ is able to intercalate reversibly both Na^+ and Li^+ ions following the chemical reaction $Li_xNa_{1-x}MnPO_4 \leftrightarrow Li_{0.0}Na_{0.5}MnPO_4$ ($0.25 \leq x \leq 0.45$).[4] However, the electrochemical performance of $NaMnPO_4$ is still far from the desired characteristics due to the lack of optimized structure and compliant electrolytes.

In order to tune the structure with respect to the Na^+ storage capacity, element substitution has widely been undertaken.[5] Among a diversity of elements, the most suitable are those ones, which stabilize the structure of electrodes in desodiated state, improve their intrinsic electronic conductivity and enhance the operating potential of alkaline ion insertion without participating in the electrochemical reaction.[1,2,6] These elements are known to be electrochemically inactive and they comprise B^{3+}, Al^{3+}, Mg^{2+}, Zr^{4+}, *etc.*[7] Magnesium is of special interest for the incorporation in the olivine structure due to its light atomic weight and identical valence state with that of the electrochemically active Mn^{2+} ions. Recently we have demonstrated that the Mg solubility in $NaMnPO_4$ is restricted up to 15 mol%.[8] This is in contrast to the lithium analogues, forming solid solutions having compositions such as $LiMn_{1-x}Mg_xPO_4$ without any concentration constrains.[9,10] The difference between Mg-substituted $NaMnPO_4$ and $LiMnPO_4$ analogues arises from their structure peculiarities.[8] For sodium manganese phospho-olivine, it is found out that Mg^{2+} occupies preferentially M1 olivine site instead of the usual M2 sites and the magnesium charges are compensated by creation of corresponding metal vacancies in the M1 position: $[Na_{1-2x/(1-x)}Mg_{x/(1-x)}]_{M1}[Mn]_{M2}PO_4$.[8] In lithium manganese phospho-olivine, Mg^{2+} ions substitute the Mn^{2+} ions, which leads to a significant improvement in the electrochemical performance of $LiMnPO_4$ due to a reduction of the lattice mismatch between the lithiated and delithiated phases, as well as to a modification of the Mn^{3+}/Mn^{2+} redox

[a]*Institute of General and Inorganic Chemistry, Bulgarian Academy of Sciences, Acad. G. Bonchev Str. Bldg. 11, 1113 Sofia, Bulgaria. E-mail: radstoy@svr.igic.bas.bg*

[b]*Institute of Mineralogy and Crystallography, Bulgarian Academy of Sciences, 1113 Sofia, Bulgaria*

† Electronic supplementary information (ESI) available: EPR spectrum; BF-STEM images and composition maps. See DOI: 10.1039/d0ra05698g

couple.[9,11] Although the electrochemical performance of $LiMnPO_4$ in lithium ion batteries is a subject of intensive studies during the last years, the properties of $NaMnPO_4$ with respect to Li^+ and Na^+ intercalation are poorly understood.

Herein the first report on the storage performance of Mg^{2+} substituted $NaMnPO_4$ is provided. The Mg substituted phospho-olivines are prepared on the basis of ionic exchange reactions involving participation of Mg-substituted $KMnPO_4 \cdot H_2O$ dittmarites as structural template.[8] In order to improve the conductivity, the phosphate particles were furthermore covered with activated carbon through ball-milling followed by thermal treatment at 400 °C. This is a standard procedure for $LiMnPO_4$ in order to achieve a Mn^{2+}/Mn^{3+} plateau at 4.1 V at high reversibility.[6] The storage performance of phospho-olivines is analyzed in sodium and lithium half-ion cells, as well as in full-ion cells *versus* bio-mass derived activated carbon and spinel $Li_4Ti_5O_{12}$ as anodes. The spinel oxide is selected since it is able to intercalate reversibly both Li^+ and Na^+ ions,[12–14] while activated carbon intercalates more easily Na^+ ions than Li^+.[15,16] The compatibility of phospho-olivines with electrolytes is assessed by utilization of several types of lithium and sodium carbonate-based solutions. Although $LiPF_6$-based electrolyte has higher conductivity, the $LiBF_4$-based electrolyte displays better thermal and hydrolytic stabilities.[17–19] The conductivities of both sodium electrolytes are comparable (7.98 *versus* 6.2 mS cm^{-1}), but the $NaPF_6$-based electrolyte is more reactive towards electrodes than the NaTFSI one.[20] To suppress the corrosion of the aluminum collector, small percentage of $NaPF_6$ salt is added to NaTFSI-based solution.[18] The structure and morphology of parent and cycled olivine phases are monitored by a combination of powder X-ray diffraction, TEM, vibrational spectroscopy and electron paramagnetic resonance spectroscopy (EPR).

2. Experimental

2.1. Synthesis

Mg-substituted $NaMnPO_4$ was obtained at 200 °C by an ion-exchange reaction using dittmarite-type of $KMn_{0.85}Mg_{0.15}PO_4 \cdot H_2O$ as a structure-directing precursor. The details are given elsewhere.[8] A reference composition $LiMn_{0.85}Mg_{0.15}PO_4$ was also prepared using the same $KMn_{0.85}Mg_{0.15}PO_4 \cdot H_2O$ precursor.[8] For comparison, non-substituted $NaMnPO_4$ was synthesized by ion-exchange from $KMnPO_4 \cdot H_2O$ as it was described previously.[4] To improve the degree of crystallinity, the as-prepared phospho-olivines were further annealed at 400 and 500 °C for sodium and lithium composition, respectively. For the sake of simplicity, the Mg-substituted $NaMnPO_4$ will be further on denoted by Mg-NMP, accordingly Mg-substituted $LiMnPO_4$ by Mg-LMP and non-substituted $NaMnPO_4$ – by NMP. The composite materials were prepared by ball-milling of Mg-NMP, NMP and Mg-LMP with 15% conductive carbon black additives Super C65 (TIMCAL) for 4 h at a speed of 300 rpm using planetary "Pulverisette 6" mill (Fritsch) with agate balls (ϕ 10 mm). The sample to balls ratio was 10 : 1. The ball-milled composites denoted by Mg-NMP/C, NMP/C and Mg-LMP/C were also thermally treated under argon flow at 400 °C for 3 h.

2.2. Composites and electrodes characterization

The powder X-ray diffraction (XRD) patterns were recorded on a Bruker Advance 8 diffractometer with LynxEye detector (CuKα radiation). The IR spectra were registered in KBr discs on a Fourier transform Nicolet Avatar-320 instrument (resolution < 2 cm^{-1}). LabRam 300 Horiba Jobin Yvon spectrometer was used to record Raman spectra (excitation with a He–Ne laser at 633 nm). The EPR spectra of Mn^{2+} ions in phospho-olivines were collected on a Bruker EMX^{plus} EPR spectrometer operating in the X-band (9.4 GHz) within a temperature range of 100–400 K. The SEM images were obtained by JEOL JSM-5510 scanning electron microscope. The TEM studied were performed on a JEOL 2100 transmission electron microscope and a JEOL 2100 XEDS: Oxford Instruments, $X\text{-}MAX^N$ 80T CCD Camera ORIUS 1000, 11 Mp, GATAN at accelerating voltage of 200 kV. The specimens were prepared by grinding and dispersing the powders in ethanol by ultrasonic treatment for 6 minutes. The suspensions were dripped onto standard holey carbon/Cu grids. The analysis was carried out by the Digital Micrograph software. The porous texture of the samples was examined by low-temperature (77.4 K) nitrogen adsorption using Quantachrome (USA) NOVA 1200e instrument. The specific surface area was evaluated by the BET method at relative pressure p/p_0 within the range of 0.10–0.30. The total pore volume is calculated according to Gurwitsch's rule at $p/p_0 = 0.99$. The pore size distribution was estimated according to Barrett–Joyner–Halenda method. The electrical resistivity, density and mobility of charge carriers were determined by a MMR's Variable Temperature Hall System (K2500-5SLP-SP) using the Van der Pauw method.

2.3. Electrochemical characterization

The storage performance was analyzed in half- and full-ion cells. The electrochemical charging–discharging curves of composites Mg-NMP/C and NMP/C were examined by using EL-CELL type of two-electrode cells, mounted in dry box under argon atmosphere. The intercalation/deintercalation cycling was carried out using an eight-channel Arbin BT2000 system in galvanostatic mode. The positive electrode, supported onto an aluminium foil, was a mixture containing 80% Mg-NMP/C (or NMP/C), 7.5% C-NERGY KS 6L graphite (TIMCAL), 7.5% Super C65 (TIMCAL) and 5% polyvinylidene fluoride (PVDF). As negative electrodes we have studied metallic lithium and sodium, bio-mass derived activated carbon and spinel $Li_4Ti_5O_{12}$. The following electrolytes were tested: 1 M $LiPF_6$ in EC/DMC, 1 M $LiBF_4$ in EC/DMC, 1 M $NaPF_6$ in PC and 1 M NaTFSI in PC containing 5% $NaPF_6$ (the latter will be denoted by NaTFSI/5$NaPF_6$). The charging and discharging rates were expressed as C/h, where h denotes the hours needed for the insertion of one alkaline ion per formula unit at the applied current intensity. The model cells were cycled at C/5, C/20, C/50 and C/100 rates.

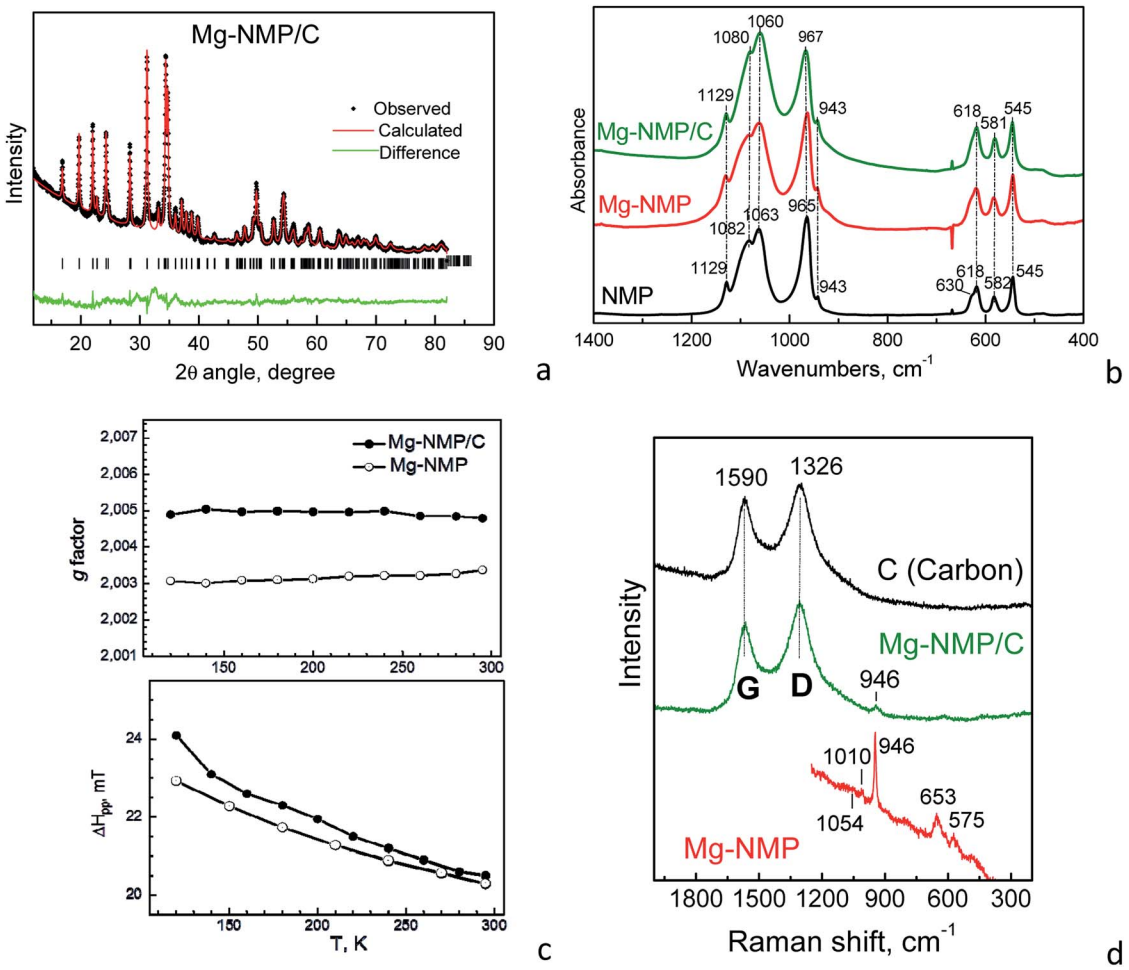

Fig. 1 XRD pattern (a), IR spectra (b), *g*-factor and EPR line width (c) and Raman spectra (d) of Mg-NMP, Mg-NMP/C and NMP.

3. Results and discussion

3.1. Composites between Mg-substituted $NaMnPO_4$ and black carbon

The Mg-substituted phase is obtained following the procedure given elsewhere.[8] To rationalize the effect of Mg^{2+} on electrochemical storage properties, the phase with a threshold Mg amount is prepared (*i.e.* $x = 0.15$ in precursor). According to the data obtained by ICP analysis, the chemical composition of the olivine phase is: 9.34 wt% Na, 34.03 wt% Mn and 2.11 wt% Mg. Although the Mg-to-Mn ratio is close to the nominal one (*i.e.* 0.14 *versus* 0.15), the Na-to-Mn ratio is lower (*i.e.* Na/Mn = 0.72). Assuming that all the Mg^{2+} ions are located on the M1 sites in the olivine structure,[8] the most probable structural formula is $[Na_{0.72}Mg_{0.14}\square_{0.14}]_{M1}[Mn]_{M2}PO_4$. In addition, the EDS data give a close composition – $[Na_{0.76}Mg_{0.12}\square_{0.12}]_{M1}[Mn]_{M2}PO_4$.

Ball-milling of Mg-NMP with carbon black leads to the formation of a composite, in which the structure of the olivine phase remains intact (Fig. 1a). The lattice parameters of parent Mg-NMP and ball-milled Mg-NMP are listed in Table 1.

Table 1 Lattice parameters of powders NMP and Mg-NMP, as well as composites NMP/C, Mg-NMP/C, Mg-LMP/C and electrodes Mg-NMP/C cycled in lithium half-cells using $LiPF_6$ and $NaPF_6$ electrolytes

				Mg-NMP/C			Mg-LMP/C
	NMP	Mg-NMP	NMP/C	Composite	Electrode cycled in $LiPF_6$	Electrode cycled in $NaPF_6$	$LiMg_{0.15}Mn_{0.85}PO_4/C$
a (Å)	10.5177(3)	10.4963(5)	10.5167(4)	10.4974(8)	10.471	10.465	10.3897(6)
b (Å)	6.3144(2)	6.2936(4)	6.3163(2)	6.3014(5)	6.285	6.320	6.0668(4)
c (Å)	4.9872(2)	4.9817(4)	4.9885(2)	4.9845(4)	4.971	4.970	4.7903(3)
V (Å^3)	331.227(22)	329.099(40)	331.378(25)	329.723(50)	327.23	328.75	298.773(37)

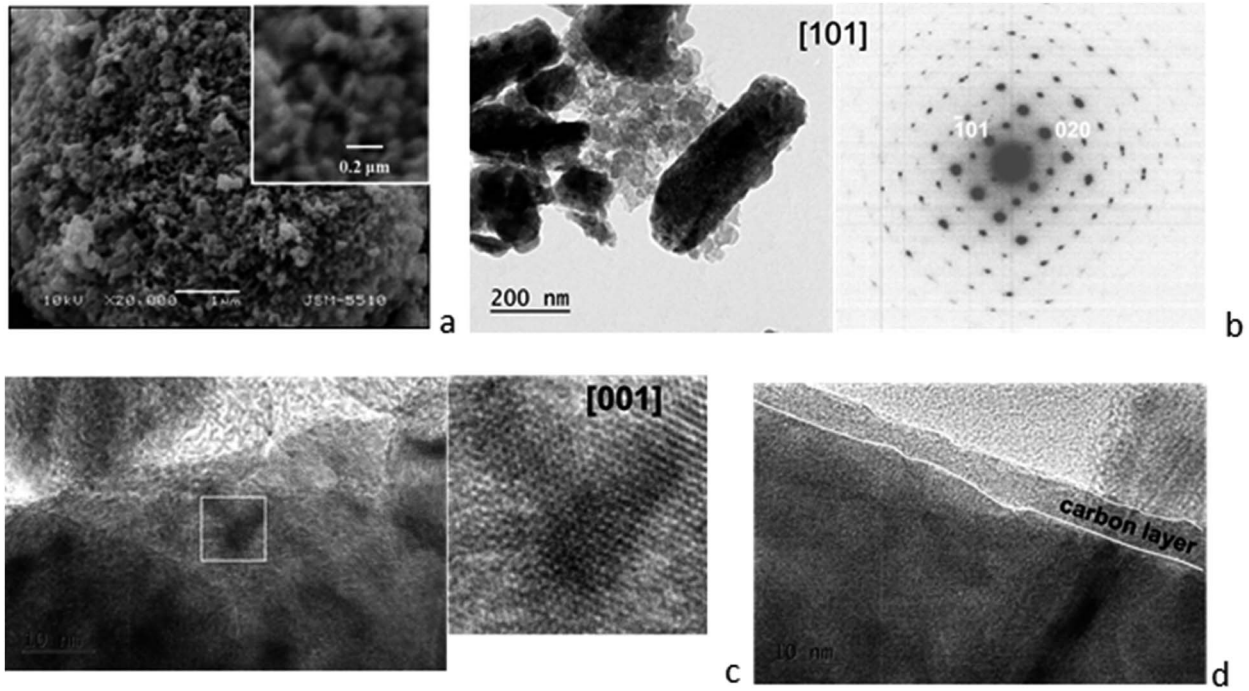

Fig. 2 Morphology of Mg-NMP/C composite: (a) SEM image; (b) bright field TEM image and corresponding SAED; (c) HRTEM image of the olivine particle; (d) HRTEM image indicating the carbon film.

The comparison shows that the lattice parameters of the parent and ball-milled phases have close values. The inertness of the olivine structure towards ball-milling is also supported by IR spectroscopy of the composites (Fig. 1b): the characteristic IR modes due to stretching and bending vibrations of PO_4^{3-} group retain their positions. Moreover, the distribution of Mg over two olivine positions is preserved as it was shown by the EPR parameters of parent and milled phases (Fig. 1c). The EPR spectrum of Mg-NMP/C composite consists of single Lorentzian line due to Mn^{2+} ions (Fig. S1†). The *g*-factor and the EPR line width of ball-milled Mg-NMP/C are similar to those of the parent phase (Fig. 1c). This fact reveals that the olivine phase does not undergo any structural transformation and the preferential Mg location in the M1 olivine sites is insensitive towards ball-milling.

The carbon network in the composite seems also to be unaffected by the milling procedure (Fig. 1d). The Raman spectra display two intensive bands at 1590 and 1326 cm^{-1}. These bands denoted as G (graphitic) and D (disorder) are typical of disordered carbon with graphite like medium-range order.[21] The positions and the ratio between areas of the two modes are maintained after grinding ($I_D/I_G = 1.75$ *versus* $I_D/I_G = 1.70$, respectively). This is an indication that the milling procedure does not create any additional defects in the carbon network.

The parameter that is altered during ball-milling is the morphology (Fig. 2). The SEM and TEM images indicate that the Mg-NMP/C composite consists of spherical aggregates, composed of closely stacked thin rod-like nanoparticles. Both the SAED and HRTEM of rod-like nanoparticles are indexed by a model including the olivine structure, thus indicating the retention of the crystallinity of Mg-NMP on a nano-scale level. The TEM images illustrates, furthermore, that the olivine particles are covered by a carbon layer with a thickness no less than 5 nm. In addition, separate carbon particles are also visible. It is worth mentioning that the same morphology has

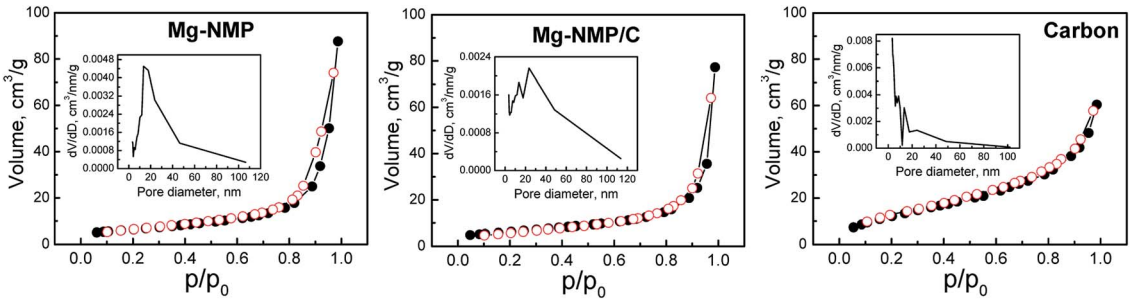

Fig. 3 Adsorption–desorption isoterms of Mg-NMP, Mg-NMP/C and carbon additive (C). The insets show pore size distribution curves.

already been observed after ball-milling of the unsubstituted $NaMnPO_4$ with carbon additives.[4] Therefore, the SEM and TEM data reveal that ball-milling is an effective way to prepare an intimate composite between Mg-NMP olivine and the carbon black additives.

The Mg-substituted phosphate Mg-NMP is a typical mesoporous material (Fig. 3), having a relatively high specific surface area of 22 $m^2\ g^{-1}$ and a total pore volume of 0.13 $cm^3\ g^{-1}$. The pore size distribution curve (Fig. 3) shows that the predominant pores fall within the range between 5 and 45 nm (average pore size being 24 nm). The carbon additive has also a mesoporous texture: the specific surface area, the total pore volume, and the average pore size amount to 49 $m^2\ g^{-1}$, 0.09 $cm^3\ g^{-1}$ and about 8 nm, respectively. After ball-milling, the composite Mg-NMP/C exhibits a slightly higher specific surface area than that of single component Mg-NMP (*i.e.* 24 *versus* 22 $m^2\ g^{-1}$), as well as the slightly lower total pore volume (0.11 $cm^3\ g^{-1}$) and average pore size (22 nm). In addition, the pores are distributed within a broader range (between 4 and 80 nm).

The microporous texture makes the composite suitable for using it as an electrode material with respect to the wetting and electrolyte penetration.

3.2. Li and Na storage in Mg-substituted $NaMnPO_4$

The important parameter for the application of the phospho-olivines as electrode materials is their electrical conductivity. In this study, we measure the electrical conductivity of the two composites: Mg-NMP/C and NMP/C. Although the accuracy is low (about 40%), the conductivity of the composite comprising Mg-substituted $NaMnPO_4$ is three orders of magnitude higher than that of the parent $NaMnPO_4$-derived composite: 2.5×10^{-6} S cm^{-1} *versus* 0.007×10^{-6} S cm^{-1}, respectively. The higher electrical conductivity of Mg-NMP/carbon appears as a result of the increased carrier density (2700×10^8 cm^{-3} *versus* 4×10^8 cm^{-3}), while the carrier mobility remains unchanged (about 100 $cm^2\ V^{-1}\ s^{-1}$). The dramatic difference in the conductivities of both composites could be related to the olivine phase and to the effect of Mg-substituent. The enhanced electrical conductivity is a prerequisite for achieving good storage performance of phospho-olivines.

Till now, the electrochemical performance of NMP has been studied in hybrid Li,Na ion cell due to the lower performance in sodium ion cell.[4] To compare the electrochemical performances of NMP and Mg-NMP, Fig. 4 gives the CV- and charge/discharge curves of parent and Mg-substituted phosphates. In the CV-curve of the parent NMP, there are one broad anodic peak between 4.4 and 4.5 followed by two cathodic peaks at 3.87 and 3.15 V. Based on previous studies,[4] the anodic peak corresponds to the desodiation of $NaMnPO_4$, while the cathodic peaks are associated with consecutive intercalation of Li^+ and Na^+ ions. In comparison with NMP, the CV-curves of Mg-substituted phospho-olivine are more structured: there are two anodic peaks at around 4.35 and 4.55 V, as well as one narrow cathodic peak at 3.79 V together with a broad peak at 2.8 V. The observation of two anodic peaks is a mark that the desodiation of Mg-NMP takes place in a different mechanism in comparison with

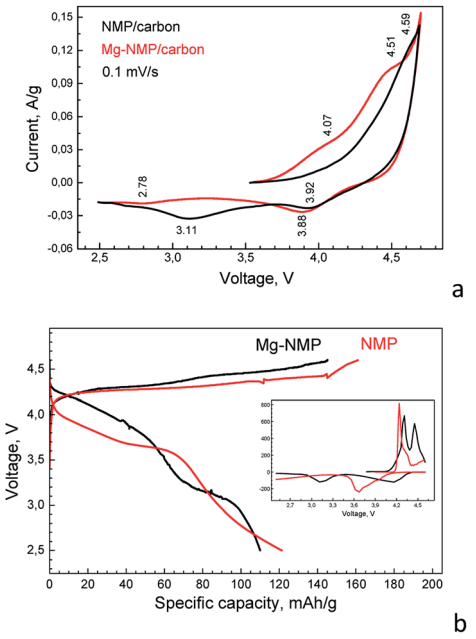

Fig. 4 CV-curves (a) and galvanostatic charge/discharge (b) curves for Mg-NMP and NMP. The cell cycling begins by anodic scan (*i.e.* by desodiation). All experiments are carried out with $LiPF_6$-based electrolyte. The inset gives the first derivatives of charge/discharge curves.

the parent NMP phase. In the reverse cathodic scan, the desodiated Mg-NMP and NMP phases seem to insert Na^+ and Li^+ by a similar manner.

The galvanostatic experiments support, furthermore, the CV-data (Fig. 4b). For the parent phase, the oxidation reaction due to the Mn^{2+}/Mn^{3+} couple occurs at 4.28 V, while the reduction peak is developed between 3.9 and 3.6 V. The appearance of Mg^{2+} ions in the olivine structure causes a change in the galvanostatic curve profiles in agreement with the CV-curves (Fig. 4a): there are two oxidation plateaus at 4.30 and 4.45 V in the charge curves and two reduction plateaus at 4.10 and 3.15 V in the discharge curve. The charge and discharge capacities slightly decrease upon Mg-substitution: from 161 to 146 mA h g^{-1} in charging, as well as from 121 mA h g^{-1} to 110 mA h g^{-1} in discharging. On the first glance, this is a consequence of the presence of Mg^{2+} ions, which are not participating in the electrochemical reaction. However, the observed decreases in the charge and discharge capacities are smaller than the expected one taking into account the Mg content (15 mol%). This provides evidence for the improved electrochemical performance of Mg-substituted phospho-olivines. In addition, the irreversible capacity for both NMP and Mg-NMP looks like similar: 40 *versus* 36 mA h g^{-1}. This corroborates that partial electrolyte decomposition at potentials higher than 4.3 V can also contribute to the charge capacity. It is worth mentioning that the electrolyte decomposition at high potentials is a common feature observed when lithium analogue $LiMnPO_4$ is cycled in $LiPF_6$-based electrolyte.[22]

The intercalation properties of Mg-NMP are dictated by the electrolyte composition. Fig. 5a compares the first charging/discharging curves of Mg-NMP in lithium and sodium

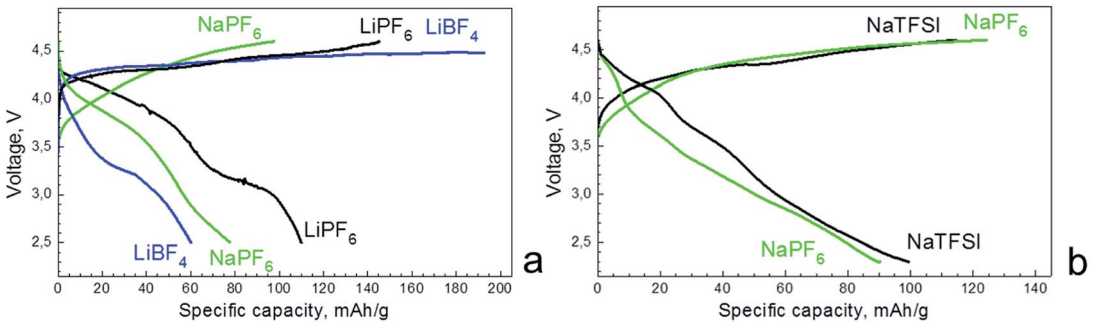

Fig. 5 Charging/discharging curves for Mg-NMP cycled in lithium (a) and sodium (b) half-cells using different carbonate-based electrolytes. The charging/discharging rate is C/100.

carbonate-based electrolytes. When $LiBF_4$-based electrolyte is used instead of $LiPF_6$, the first charging capacity increases significantly: 200 mA h g^{-1} *versus* 146 mA h g^{-1}. Moreover, the charging capacity exceeds the theoretical one (*i.e.* 134 mA h g^{-1} for 15% Mg-substituted NMP). This fact indicates that $LiBF_4$-containing electrolyte undergoes more significant decomposition in comparison with that of the $LiPF_6$-based electrolyte. During the reverse cell cycling, the discharging capacity in $LiBF_4$-containing electrolyte becomes nearly two times lower than that in the $LiPF_6$ electrolyte. The loss of the discharging capacity is concomitant with a change in the discharging curve profile: only one reduction plateau at about 3.2 V is visible when $LiBF_4$-electrolyte is used. This evidences that Mg-NMP exhibits worse electrochemical performance in the $LiBF_4$-based electrolyte than that containing $LiPF_6$. The reduction in the performance of Mg-NMP can be related to lower conductivity of $LiBF_4$-containing electrolyte, as well as to more intensive electrode–electrolyte interaction at potentials higher than 4.3 V.

In sodium electrolytes, the charging curve of Mg-NMP in lithium half-cell does not show any distinct plateau and the capacity reaches a value of 97 mA h g^{-1}. To the contrary, the discharge curve displays one plateau at 3.9 V and the discharging capacity is of 78 mA h g^{-1}. The comparison indicates that, in lithium half-cell, the storage performance of Mg-NMP is worse in the sodium electrolytes than the lithium electrolyte containing $LiPF_6$. This can be explained in terms of dual Li^+,Na^+ intercalation into olivine phase, which proceeds more easily in the lithium electrolyte. The intercalation mechanism will be discussed later.

In sodium half-cell, the charging of Mg-NMP leads to a deintercalation of all Na^+ ions from the structural formula (*i.e.* $[Na_{0.76}Mg_{0.12}\square_{0.12}]_{M1}[Mn]_{M2}PO_4$, the corresponding capacity is of 120–125 mA h g^{-1}, Fig. 5b). During the reverse process of discharging, 0.63 mol Na^+ ions are intercalated into desodiated phase (corresponding capacity of 95–100 mA h g^{-1}). Although the charging and discharging capacities marginally depend on the electrolyte composition, the galvanostatic curves are more structured in NaTFSI/5$NaPF_6$ than that in $NaPF_6$-based electrolyte. In NaTFSI/5$NaPF_6$ electrolyte, the charging curve displays a smooth increase up to 4.6 V, while in the discharging curve, two plateaus at 4.15 and 3.61 V are clearly resolved. On one hand, this discloses that NaTFSI/5$NaPF_6$-based electrolyte is most suitable to unveil the electrochemical properties of the phospho-olivine phase in comparison with pure $NaPF_6$ electrolyte irrespective of their close solution conductivities. On the other hand, the structured discharging curve implies that the Na^+ intercalation into Mg-NMP is, most probably, a two-step process with a formation of distinct sodium-deficient phases. It is worth mentioning that, till now, the multi-phase

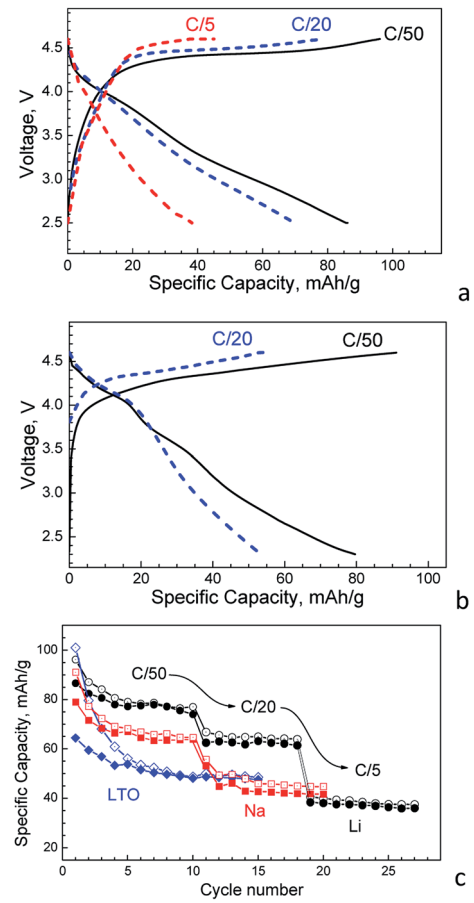

Fig. 6 Charging/discharging curves for Mg-NMP cycled in: (a) lithium half-cell using $LiPF_6$-based electrolyte; (b) sodium half-cell using NaTFSI/5$NaPF_6$-based electrolyte; (c) rate capability of Mg-NMP in lithium and sodium half-cells (black and red symbols, respectively) and full-ion cells with $Li_4Ti_5O_{12}$ anode (blue symbols). Open and full symbols correspond to the charging and discharging capacity, respectively.

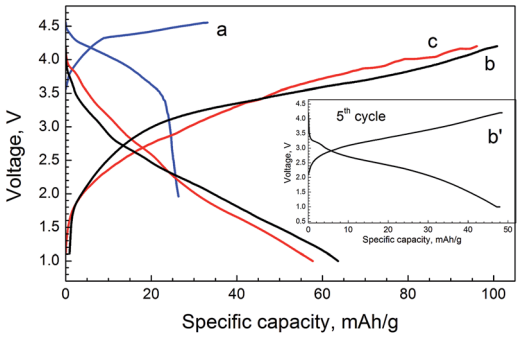

Fig. 7 First charging/discharging curves for Mg-NMP cycled in a full-ion cell *versus* anode comprising biomass-derived activated carbon (a) and $Li_4Ti_5O_{12}$ spinel (b and c). The cell operates with $NaPF_6$-based electrolytes (a and c) and $LiPF_6$-based one (b). The inset shows the charging/discharging curves after 5 cycles (b').

mechanism of Na^+ intercalation into olivine structure has only been established in the case of the iron analogue $NaFePO_4$.[23,24] The extraction of Na^+ from $NaFePO_4$ leading to $FePO_4$ proceeds through two-step reaction *via* formation of $Na_{2/3}FePO_4$. Although the desodiation is a two-step reaction, the reverse of sodiation of $FePO_4$ is a complex process, including the occurrence of three phases with varying miscibility limits.[20] Similar to $NaFePO_4$, it appears that the Mg-substituted $NaMnPO_4$ undergoes multi-phase transformation during the Na^+ intercalation. It is interesting to note that, using the same protocol of electrode fabrication, the parent phase $NaMnPO_4$ is electrochemically inactive in sodium half-cell. This reveals once again the positive impact of Mg substituents on the electrochemical properties of $NaMnPO_4$.

In summary, Mg-NMP delivers higher capacity in the lithium half-cell than that of the sodium half-cell: the charging and discharging capacities are 146 and 110 mA h g^{-1}, respectively (Fig. 5). This observation reveals that Li^+ intercalation, in addition to Na^+ intercalation, takes place when Mg-NMP operates in lithium half-cell. Among different electrolyte compositions, the most appropriate is $LiPF_6$-based electrolyte. Therefore, the rate capability of Mg-NMP is examined in the $LiPF_6$ electrolyte.

Fig. 6 shows the charging/discharging curves of Mg-NMP in dependence on the C-rate. By increasing the C-rate from C/50 to C/5, the two plateaus in both the charging and discharging curves are coalesced. In the same order, the specific capacity decreases. However, even at the faster C-rate, the capacity is still relatively high (*i.e.* about 40 mA h g^{-1}). It is noticeable that this rate capability is achieved without any optimization of the Al collector and separator. In comparison with lithium half-cell, the sodium half-cell delivers lower capacity irrespective of the C-rate (Fig. 6b and c). In addition, the rate capability in the sodium half-cell seems also worse (Fig. 6b and c). This observation corroborates with a dual Li^+,Na^+ intercalation taking place in the lithium half-cell.

The storage performance of Mg-NMP is quantified in a full-ion cell, where metallic alkaline anode is replaced by bio-mass derived activated carbon. The activated carbon has been shown to store easily Na^+ ions.[15,16] That is why, the full-ion cell is constructed by application of $NaPF_6$-based electrolyte. The first charging/discharging curves of the full-ion cell are given in Fig. 7. As one can see, there are well-resolved oxidation and reduction plateaus at 4.3 and 4.0 V, respectively. These plateaus originate from the Na^+ insertion and extraction from Mg-NMP. The charging and discharging capacities associated with Na^+ intercalation are low.

In order to increase the specific capacity, the full cell is constructed with $Li_4Ti_5O_{12}$ spinel as an anode instead of the activated carbon (Fig. 7). It has been found out that $Li_4Ti_5O_{12}$ spinel exhibits non-selective intercalation properties and it is able to intercalate reversibly Li^+ and Na^+ ions at a flat voltage plateau of 1.55 V *versus* Li/Li^+ and at 0.91 V *versus* Na/Na^+.[25,26]

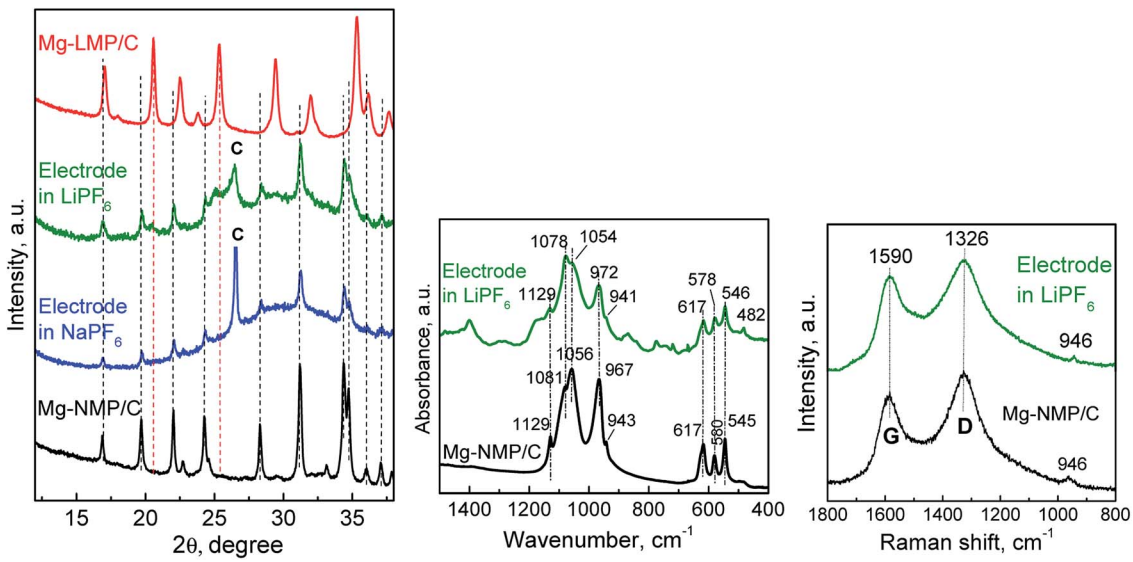

Fig. 8 XRD patterns (left), IR spectra (middle) and Raman spectra (right) of Mg-NMP/C and electrodes cycled in $LiPF_6$ and $NaPF_6$ electrolytes *versus* Li metal as anode.

That is why $Li_4Ti_5O_{12}$ is used as an anode. In $LiPF_6$-containing electrolyte, both charging and discharging curves display smooth profiles without any plateaus. The same picture is observed when $LiPF_6$ is replaced with $NaPF_6$-containing electrolyte. Moreover, the charging and discharging capacities are also close (Fig. 7). The first irreversible capacity is about 40 mA h g^{-1}, which diminishes quickly (Fig. 7). After 5 cycles, the coulombic efficiency is nearly 99% (Fig. 7). The full-ion cell operates at an average voltage of 2.5 V and it delivers a reversible capacity of about 50 mA h g^{-1}. It is noticeable that the full-ion cell comprising Mg-NMP and $Li_4Ti_5O_{12}$ electrodes delivers higher capacity in comparison with that composed of Mg-NMP and activated carbon electrodes. This can be related to dual Li^+,Na^+ and single Na^+ intercalation proceeding in Mg-NMP, when it is paired with $Li_4Ti_5O_{12}$ or activated carbon as anodes.

3.3. Intercalation capacity of Mg-substituted $NaMnPO_4$

To rationalize the storage properties of Mg-NMP, the structure and morphology of the Mg-NMP electrode are reevaluated. The subject of this study is the Mg-NMP cycled in a half-ion cell with $LiPF_6$- and $NaPF_6$-based electrolytes between 2.5 and 4.6 V for 10 cycles and recovered from the cells in discharged state (*i.e.* at 2.5 V). The XRD pattern of cycled Mg-NMP displays the diffraction peaks due to the olivine structure (Fig. 8). The lattice parameters tend to decrease especially in the case, when $LiPF_6$-based electrolyte is used (Table 1). The volume cell contraction implies that the composition of Mg-NMP is not recovered after the electrochemical reaction. This is a consequence of a partial extraction of Na^+ from Mg-NMP. However, an exchange of bigger Na^+ ions with smaller Li^+ ions cannot be rejected. For the sake of comparison, the lattice parameters for 15% Mg-substituted $LiMnPO_4$ is also given in Table 1. The comparison shows that the lattice parameters of cycled Mg-NMP are intermediate between that of the sodium and lithium analogues, being closer to the sodium side.

The IR spectra of cycled Mg-NMP reveal a stability of the olivine structure after the electrochemical reaction: the characteristic bands due to PO_4^{3-} vibrations match those of the pristine composition (Fig. 8). The new feature of the IR spectrum of Mg-NMP cycled in $LiPF_6$ is the appearance of a peak in the region below 500 cm^{-1}. This is the region, where usually the Li–O vibrations occur. For example, the IR spectrum of the lithium analogue $LiMnPO_4$ displays two bands at 500 and 458 cm^{-1} in this region.[8] Therefore, the new peak at 482 cm^{-1} for cycled Mg-NMP can be assigned to Li–O vibrations. This means that IR spectroscopy bears witness to an exchange of Na^+ with Li^+ during the electrochemical reaction rather than the formation of Na^+ deficient phospho-olivine. It is of importance that the electrochemical reaction exerts influence on the structure of the Mg-NMP, while the carbon network remains intact as it is demonstrated by Raman spectra (Fig. 8). The D- and G-bands retain their positions, as well as the intensity ratio between the two bands is also constant ($I_D/I_G = 1.71$ for the cycled electrode).

The TEM analysis shed further light on the storage properties of cycled Mg-NMP (Fig. 9). After the electrochemical reaction, the morphology of Mg-NMP is preserved to a great extent (see Fig. 2). In the lithium electrolyte, the polycrystalline diffraction of cycled Mg-NMP corresponds to a phase mixture of the olivine phase and carbonaceous additives (Fig. 9a). The HR-TEM image reveals that Mg-NMP is composed of nano-domains, where the lattice fringes due to lithium and sodium phospho-olivine structure can be clearly distinguished (Fig. 9b). (It is worth recalling that the HRTEM images are calculated and compared with the lattice parameters of the lithium and sodium phospho-olivine analogues given in Table 1.) In the sodium electrolyte, both the SAED and HR-TEM images of cycled Mg-NMP signify a preservation of the sodium phospho-olivine structure on a nano-level scale (Fig. 9c and d). Moreover, the nano-domains due to lithium phospho-olivine are very rarely observed in comparison with Mg-NMP cycled in lithium electrolyte (Fig. 9). The TEM data coincide with the storage capacity determined in lithium and sodium electrolyte (Fig. 6).

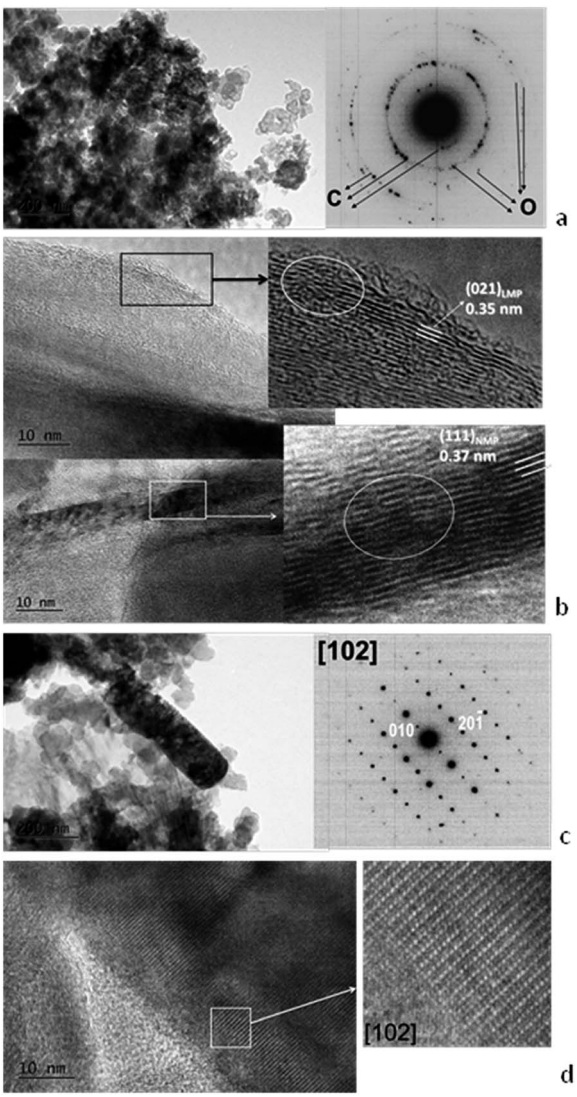

Fig. 9 Bright field, SAED and HRTEM images of: Mg-NMP/C electrode cycled in $LiPF_6$ electrolyte (a and b) and Mg-NMP/C electrode cycled in $NaPF_6$ electrolyte (c and d).

Table 2 Elemental composition determined using high angle annular dark field STEM images

Electrode	Mg/(Mn + Mg)	Na/(Mn + Mg)	P/(Mn + Mg)	F/(Mn + Mg)
Pristine	0.12	0.76	0.90	0.0
Mg-NMP (in $LiPF_6$)	0.11	0.20	1.29[a]	1.09[a]
Mg-NMP (in $NaPF_6$)	0.13	0.49	0.97[a]	0.09[a]

[a] Electrolyte decomposition.

The composition of cycled Mg-NMP in both electrolytes is calculated on the basis of BF-STEM and the data are listed in Table 2. The corresponding composition maps are represented in Fig. S2–S4.† Two features can be outlined. First, the content of Mg and P elements is constant, which confirms, once again, the stability of the phospho-olivine in lithium and sodium electrolytes. In contrast to Mg and P, the content of Na element decreases in comparison with that of the pristine composition. This decrease is more significant when Mg-NMP cycles in the lithium electrolyte. It is worth mentioning that this technique should not be used for the determination the content of Li element. Irrespective of this, the observed decrease in the sodium content implies an accomplishment of dual intercalation of Li^+,Na^+, which proceeds more easily in the lithium electrolyte. In addition, the cycled electrodes contain also F elements. The occurrence of fluorine is a result of the using PVDF during electrode fabrication. However, the F content exceeds the set amount of PVDF, if the lithium electrolyte is applied. This can be related with an easier adsorption of $LiPF_6$ than that of $NaPF_6$. This is an interesting fact, which deserves further studies. On the other side, this fact underlines the sensitivity of Mg-NMP towards the electrolyte composition.

Another aspect of the cycled electrode is the cationic distribution of Mg inside the olivine structure. The EPR spectroscopy allows getting insight into cationic distribution. When diamagnetic Mg^{2+} ions substitute the paramagnetic Mn^{2+} in the olivine structure, the Mn^{2+} magnetic network is diluted, thus provoking a strong broadening of the EPR signal. This picture is observed for Mg-substituted $LiMnPO_4$ (Fig. 10).

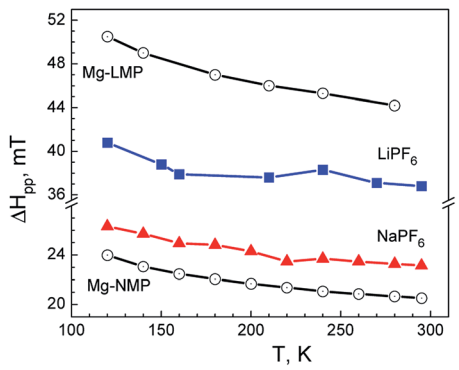

Fig. 10 EPR line width for Mg-NMP/C electrode cycled in a lithium half-ion cell with lithium and sodium electrolyte (full symbols). The open symbols correspond to the composites containing 15% Mg-substituted $LiMnPO_4$ (Mg-LNM) and $NaMnPO_4$ (Mg-NMP).

On the contrary, the presence of Mg^{2+} in the Na^+-positions instead of the Mn^{2+}-sites has a relatively slight impact on the Mn^{2+} magnetic network, as a result of which the EPR signal does not undergo any significant change. This picture is observed for Mg-substituted $NaMnPO_4$ (Fig. 10). The observed difference in the EPR line width depending on the Mg^{2+} distribution can be used as an experimental measure. After the electrochemical reaction, the EPR spectra display only one single Lorentzian line irrespective of the electrolyte composition. The EPR line width increases especially in the case of the used lithium electrolyte. This is a clear indication for the alteration of the Mn^{2+} magnetic network after the electrochemical reaction. Taking into account the TEM data, it appears that both lithium and sodium nano-domains give rise to the EPR signal, resulting in an averaging of the EPR line width. From EPR point of view, the distribution of Mg^{2+} in these nano-domains is different: in lithium nano-domains, Mg^{2+} ions substitute the Mn^{2+} ions, while in the sodium nano-domains, Mg^{2+} ions are in the sodium position. This means that the dual intercalation of Li^+ and Na^+ ions is concomitant with a Mg^{2+} redistribution inside the olivine structure. Because of the nano-scale level, the cationic mobility becomes possible.

4. Conclusions

The Mg substituents strongly modify the olivine structure of $NaMnPO_4$ due to the occupancy of the sodium positions instead of the manganese positions. Ball-milling of Mg-NMP and carbon black yields an intimate composite between them without affecting the structure of the olivine phase and of the carbon network. The composite has a conductivity of 2.5×10^{-6} S cm^{-1}, which enables to achieve a good storage performance of the phospho-olivine phase. In sodium half-cell, the compatibility of Mg-NMP and NaTFSI/5$NaPF_6$-based electrolyte is better than that of the $NaPF_6$-electrolyte. The intercalation of Na^+ into Mg-NMP proceeds through multi-phase mechanism, reaching a capacity of about 90–100 mA h g^{-1}. The storage performance of Mg-NMP is improved in lithium half-cell by using $LiPF_6$-electrolyte. The function of Mg-NMP in lithium half-cell relies on dual Li^+,Na^+ intercalation that encompasses nano-domains, in which Mg^{2+} ions are redistributed inside the olivine structure. As a result, Mg-NMP delivers higher specific capacity, as well as a good rate capability.

The full-cell constructed with $Li_4Ti_5O_{12}$ as an anode exceeds the performance of the full-cell with activated carbon as an anode. This cell operates at an average voltage of 2.5 V and delivers a reversible capacity amounting to 50 mA h g^{-1}. In general, the full ion cell does not exceed the performance of the half-ion cell. However, this is a first report on the construction of the full ion cell based on sodium manganese phospho-olivine and $Li_4Ti_5O_{12}$ electrodes with relatively acceptable behaviour.

Conflicts of interest

There are no conflicts to declare.

Acknowledgements

The authors are grateful for the financial support by the National Science Fund of Bulgaria (Project AlterIons DN09/13). Open access is financed by the National Research Program "Low Carbon Energy for the Transport and Household (E+)" (DO1-214/28.11.2018), granted by the Bulgarian Ministry of Education and Science.

References

1 Q. Ni, Y. Bai, F. Wu and C. Wu, Polyanion-type electrode materials for sodium-ion batteries, *Adv. Sci.*, 2017, **4**, 1600275.

2 T. Jin, H. Li, K. Zhu, P.-F. Wang, P. Liu and L. Jiao, Polyanion-type cathode materials for sodium-ion batteries, *Chem. Soc. Rev.*, 2020, **49**, 2342.

3 H. Kim, G. Yoon, I. Park, K.-Y. Park, B. Lee, J. Kim, Y.-U. Park, S.-K. Jung, H.-D. Lim, D. Ahn, S. Lee and K. Kang, Anomalous Jahn–Teller behavior in a manganese-based mixed-phosphate cathode for sodium ion batteries, *Energy Environ. Sci.*, 2015, **8**, 3325.

4 T. Boyadzhieva, V. Koleva, E. Zhecheva, D. Nihtianova, L. Mihaylov and R. Stoyanova, Competitive lithium and sodium intercalation into sodium manganese phospho-olivine $NaMnPO_4$ covered with carbon black, *RSC Adv.*, 2015, **5**, 87694.

5 J.-Y. Hwang, S.-T. Myung and Y.-K. Sun, Sodium-ion batteries: present and future, *Chem. Soc. Rev.*, 2017, **46**, 3529.

6 V. Aravindan, J. Gnanaraj, Y.-S. Lee and S. Madhavi, $LiMnPO_4$ – A next generation cathode material for lithium-ion batteries, *J. Mater. Chem. A*, 2013, **1**, 3518.

7 M. S. Whittingham, Lithium batteries and cathode materials, *Chem. Rev.*, 2004, **104**, 4271.

8 T. Boyadzhieva, V. Koleva and R. Stoyanova, Crystal chemistry of Mg substitution in $NaMnPO_4$ olivine: concentration limit and cation distribution, *Phys. Chem. Chem. Phys.*, 2017, **19**, 12730.

9 Y. Dong, H. Xie, J. Song, M. Xu, Y. Zhao and J. B. Goodenough, The prepared and electrochemical property of Mg doped $LiMnPO_4$ nanoplates as cathode materials for lithium-ion batteries, *J. Electrochem. Soc.*, 2012, **159**, A995.

10 V. Ramar and P. Balaya, Enhancing the electrochemical kinetics of high voltage olivine $LiMnPO_4$ by isovalent co-doping, *Phys. Chem. Chem. Phys.*, 2013, **15**, 17240.

11 G. Yang, H. Ni, H. Liu, P. Gao, H. Ji, S. Roy, J. Pinto and X. Jiang, The doping effect on the crystal structure and electrochemical properties of $LiMn_xM_{1-x}PO_4$ (M = Mg, V, Fe, Co, Gd), *J. Power Sources*, 2011, **196**, 4747.

12 R. Stoyanova, V. Koleva and A. Stoyanova, Lithium versus mono/polyvalent ion intercalation: hybrid metal ion systems for energy storage, *Chem. Rec.*, 2019, **19**, 474.

13 Y. Sun, L. Zhao, H. Pan, X. Lu, L. Gu, Y.-S. Hu, H. Li, M. Armand, Y. Ikuhara, L. Chen and X. Huang, Direct atomic-scale confirmation of three-phase storage mechanism in $Li_4Ti_5O_{12}$ anodes for room-temperature sodium-ion batteries, *Nat. Commun.*, 2013, **4**, 1870.

14 X. Yu, H. Pan, W. Wan, C. Ma, J. Bai, Q. Meng, S. N. Ehrlich, Y. S. Hu and X. Q. Yang, A size-dependent sodium storage mechanism in $Li_4Ti_5O_{12}$ investigated by a novel characterization technique combining in situ X-ray diffraction and chemical sodiation, *Nano Lett.*, 2013, **13**, 4721.

15 Q. Li, Y. Zhu, P. Zhao, C. Yuan, M. Chen and C. Wang, Commercial activated carbon as a novel precursor of the amorphous carbon for high-performance sodium-ion batteries anode, *Carbon*, 2018, **129**, 85.

16 K. Kim, D. G. Lim, C. W. Han, S. Osswald, V. Ortalan, J. P. Youngblood and V. G. Pol, Tailored carbon anodes derived from biomass for sodium-ion storage, *ACS Sustainable Chem. Eng.*, 2017, **5**, 8720.

17 B. Ravdel, K. Abraham, R. Gitzendanner, J. DiCarlo, B. Lucht and C. Campion, Thermal stability of lithium-ion battery electrolytes, *J. Power Sources*, 2003, **119–121**, 805.

18 S. S. Zhang, K. Xu and T. R. Jow, An improved electrolyte for the $LiFePO_4$ cathode working in a wide temperature range, *J. Power Sources*, 2006, **159**, 702.

19 C. L. Campion, W. Li and B. L. Lucht, Thermal decomposition of $LiPF_6$-based electrolytes for lithium-ion batteries, *J. Electrochem. Soc.*, 2005, **152**, A2327.

20 A. Ponrouch, E. Marchante, M. Courty, J.-M. Tarascon and M. Rosa Palacín, In search of an optimized electrolyte for Na-ion batteries, *Energy Environ. Sci.*, 2012, **5**, 8572.

21 F. Tuinstra and J. L. Koenig, Raman spectrum of graphite, *J. Chem. Phys.*, 1970, **53**, 1126.

22 G. Li, H. Azuma and M. Tohda, $LiMnPO_4$ as the cathode for lithium batteries, *Electrochem. Solid-State Lett.*, 2002, **5**, A135.

23 M. Galceran, D. Saurel, B. Acebedo, V. V. Roddatis, E. Martin, T. Rojo and M. Casas-Cabanas, The mechanism of $NaFePO_4$ (de)sodiation determined by *in situ* X-ray diffraction, *Phys. Chem. Chem. Phys.*, 2014, **16**, 8837.

24 J. Gaubicher, F. Boucher, P. Moreau, M. Cuisinier, P. Soudan, E. Elkaim and D. Guyomard, Abnormal operando structural behavior of sodium battery material: influence of dynamic on phase diagram of Na_xFePO_4, *Electrochem. Commun.*, 2014, **38**, 104.

25 T. Ohzuku, A. Ueda and N. Yamamoto, Zero-strain insertion material of $Li[Li_{1/3}Ti_{5/3}]O_4$ for rechargeable lithium cells, *J. Electrochem. Soc.*, 1995, **142**, 1431.

26 Y. Sun, L. Zhao, H. Pan, X. Lu, L. Gu, Y.-S. Hu, H. Li, M. Armand, Y. Ikuhara, L. Chen and X. Huang, Direct atomic-scale confirmation of three-phase storage mechanism in $Li_4Ti_5O_{12}$ anodes for room-temperature sodium-ion batteries, *Nat. Commun.*, 2013, **4**, 1870.

